Computational Fluid Dynamics JOURNAL vol.8 no.1 April 1999 (pp.56-68)
Special Issue "CIP Method" Edited by T. Yabe and T. Utsumi

NUMERICAL MHD SIMULATION OF ASTROPHYSICAL PROBLEMS BY USING CIP-MOCCT METHOD

Takahiro KUDOH† **Ryoji MATSUMOTO‡** **Kazunari SHIBATA♯**

Abstract

We present the results of astrophysical magnetohydrodynamic(MHD) simulations by using CIP method and MOC-CT method. The magnetic induction equation is solved by MOC-CT and the others by CIP. We compare our code to the Lax-Wendroff method which was popular among astrophysical MHD simulations. Our code has advantages;

(1) it can trace the contact discontinuity sharply,

(2) it keeps more stable even if the magnetic pressure is much greater than the gas pressure. We present the 1.5D simulations of solar spicules, and the 1.5D and 2.5D simulations of jet formation from accretion disks.

1 INTRODUCTION

MHD numerical simulation is the powerful method to understand the magnetohydrodynamic phenomena in the universe. MHD numerical simulations have been performed for the solar jets and flares [1, 2, 3], protostellar flares [4], jets from young stellar objects (YSO) [5, 6, 7], jets from active galactic nuclei (AGN) [8], the origin of the galactic hot plasma [9], and so on. However, numerical schemes of MHD have not been established compared to the hydrodynamical schemes. Although the modern high-resolution shock-capturing methods and their application for gasdynamic problems can be found in Hirsh [10], the extension of these schemes to equations of magnetohydrodynamics is not straightforward. Several different approximate solvers [11, 12, 13] applied to MHD equations are now at the stage of investigation and comparison.

In this paper, we introduce more economical and practical MHD scheme using CIP method [14, 15] and MOC-CT method [16, 17]. We belive that it is useful to astrophysical MHD problems. In section 2, we introduce the numerical method and show test problems. Section 3 is devoted to the applications to astrophysical problems, such as solar spicules and jets from accretion disks. We compare our code with the Lax-Wendroff method by using the results from the simulation of jets. In section 4, conclusion is described. Brief introduction of the CIP and MOC-CT method is given in Appendix.

Received on April 3, 1999

† Research Fellow of the Japan Society for the Promotion of Science, National Astronomical Observatory of Japan; Mitaka, Tokyo, 181-8588, Japan , e-mail: kudo@solar.mtk.nao.ac.jp

‡ Department of Physics, Faculty of Science, Chiba University ; e-mail: matumoto@c.chiba-u.ac.jp

♯ National Astronomical Observatory of Japan ; e-mail: shibata@solar.mtk.nao.ac.jp

2 NUMERICAL METHOD

2.1 Basic Equations

The basic equations we use are the ideal MHD equations in cgs units;

the equation of continuity;

$$\frac{\partial \rho}{\partial t} + \boldsymbol{v} \cdot \nabla \rho = -\rho \nabla \cdot \boldsymbol{v}, \tag{1}$$

the equation of motion

$$\frac{\partial \boldsymbol{v}}{\partial t} + \boldsymbol{v} \cdot \nabla \boldsymbol{v} = -\frac{1}{\rho}\nabla p + \frac{1}{4\pi\rho}(\nabla \times \boldsymbol{B}) \times \boldsymbol{B} - \nabla \Psi, \tag{2}$$

the equation of energy

$$\frac{\partial e}{\partial t} + \boldsymbol{v} \cdot \nabla e = -(\frac{p}{\rho})\nabla \cdot \boldsymbol{v}, \tag{3}$$

the equation of state for the ideal gas;

$$e = \frac{p}{(\gamma - 1)\rho}, \tag{4}$$

the magnetic induction equations;

$$\frac{\partial \boldsymbol{B}}{\partial t} = \nabla \times (\boldsymbol{v} \times \boldsymbol{B}), \tag{5}$$

where Ψ is the gravitational potential. Other variables are summarized in Table 1.

UNITS FOR NORMALIZATION

Physical quantities		Normalization unit
t	Time	r_0/V_0
r	Length	r_0
ρ	Density	ρ_0
p	Pressure	$\rho_0 V_0^2$
$\boldsymbol{v}$	Velocity	V_0
$\boldsymbol{B}$	Magnetic field	$\sqrt{\rho_0 V_0^2}$
e	Specific internal energy	V_0^2

Table 1: Physical quantities and their normalization, where r_0, ρ_0 and V_0 are typical length, density and velocity, respectively.

2.2 Numerical Schemes

The numerical schemes we use are the CIP (Cubic Interpolated Propagation) method [14, 15] and the MOC-CT (Method of Characteristic-Constrained Transport) method [16, 17].

The CIP method is applied to advection phase (the left hand sides) of the equations (1)-(3) after solving the right hand sides of the equations by using finite difference method (non-advection phase). The numerical viscosity is added to the pressure term as shown in Yabe & Aoki [14], which is only sensitive to compression.

The magnetic induction equations (5) are solved by MOC-CT to calculate the magnetic field. The MOC-CT is based on the constrained transport (CT) formalism [18] for directly evolving the magnetic field while maintaining $\nabla \cdot \boldsymbol{B} = 0$ constraint. The method of characteristics (MOC) for the Alfvén waves are used in the CT formalism to allow stable treatment of discontinuous Alfvén waves.

The flow chart of our CIP-MOC-CT scheme are summarized in Fig.1, and the formalisms of CIP, CT, and MOC method are briefly introduced in Appendix.

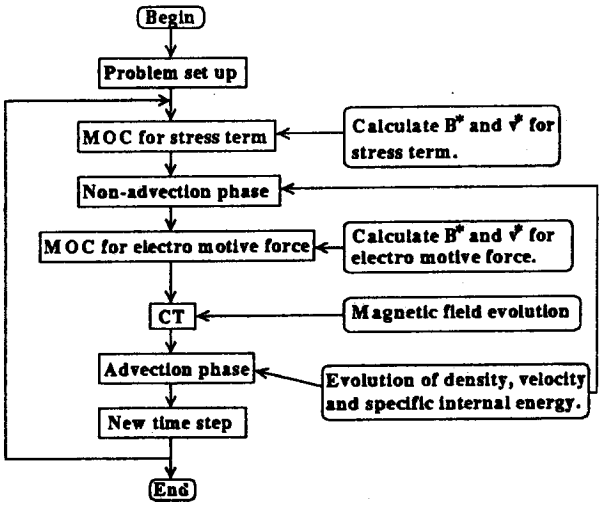

Fig.1: Schematic chart of our scheme

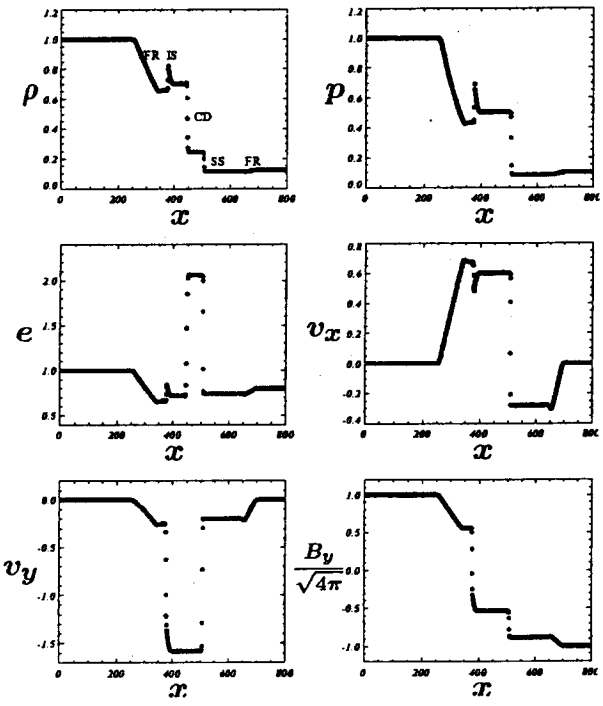

Fig.2: Magnetic shock tube results. The density (ρ), x-component of velocity (v_x), y-component of velocity (v_y), and y-component of magnetic field ($B_y/\sqrt{4\pi}$) are shown.

2.3 Test Problems

2.3.1 MHD shock tube

The MHD shock tube problem introduced by Brio & Wu [19] is often used to compare one's MHD scheme with another's.

The Cartesian coordinate is used. The number of grid points is 800, and the grid size is taken to be $\Delta x = 1$. The specific heat ratio is assumed to be $\gamma = 2$. As the initial condition, the density, pressure, and x- and y- components of magnetic field in the left state ($x < 400$) are chosen to be $\rho = 1.0$, $p = 1.0$, $B_x/\sqrt{4\pi} = 0.75$, and $B_y/\sqrt{4\pi} = 1.0$, respectively, while in the right state ($x > 400$) they are chosen to be $\rho = 0.125$, $p = 0.1$, $B_x/\sqrt{4\pi} = 0.75$, and $B_y/\sqrt{4\pi} = -1.0$. The result at $t = 80$ of the density, pressure, specific internal energy, x- and y- components of velocities, and y-component of magnetic field are shown in Fig.2. The solution consists of, from left to right, a fast rarefaction wave (FR), an intermediate shock (IS), a contact discontinuity with values on the left (CD_l), and right (CD_r), a slow shock (SS), and another fast rarefaction wave (FR). The intermediate shock should be replaced by a rotational discontinuity if the ideal MHD is exactly satisfied. Since numerical resistivity depending on grid sizes or schemes are inevitable in numerical simulations, intermediate shocks appear at the location of rotational discontinuities [20, 21].

Unlike the Sod shock tube, this MHD Riemann problem has no known analytical solution. Brio & Wu [19] present numerical solutions to this problem by using a second order upwind Roe-type scheme. Graphically, our results compare very favorably to results given by their scheme, and also by other schemes [22, 16, 23, 24, 21]. It shows that the contact discontinuity is described with fewer grid points than others. The quantitative values obtained in the run are listed in Table 2 together with values given by Stone et al. [25] and Brio & Wu [19].

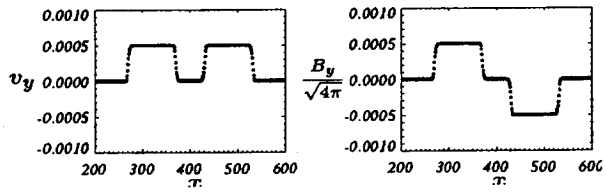

Fig.3: The propagation of a linear shear Alfvén wave. The y-component of velocity (v_y), and y-component of magnetic field ($B_y/\sqrt{4\pi}$) are shown.

2.3.2 Linear Alfvén wave

As the initial condition, y-components of velocity is chosen to be $v_y = 0.001$ ($350 < x < 450$), and $v_y = 0.0$ ($x < 350$, $x > 450$). The density, pressure, x-component of velocity, and x- and y- components of magnetic field are $\rho = 1.0$, $p = 1.0$, $v_x = 0.0$, $B_x/\sqrt{4\pi} = 1.0$, and $B_y/\sqrt{4\pi} = 0.0$, respectively. The result at $t = 80$ of y-component of velocity and y-component of magnetic field are shown in Fig.3. The MOC (method of characteristics) has a merit that it allows the propagation of the discontinuous Alfvén waves without oscillations. If the magnetic induction equation and the stress terms in the momentum equation are approximated with a simple finite central difference, the linear discontinuous Alfvén wave causes numerical oscillations. This is one of the reasons we calculate the magnetic induction equation with MOCCT.

3 APPLICATION TO ASTROPHYSICAL PROBLEM

3.1 Simulations of Solar Spicules

Spicules are one of the dynamic phenomena in quiet regions of the solar atmosphere [26]. They are jets emanating from supergranulation boundaries which trace magnetic field lines. As a model of spicules, Suematsu et al. [27] considered gasdynamic shocks (i.e., slow mode MHD shocks) which propagate along a magnetic flux tube. They suggested that the elevated, upward-moving chromospheric material is observed as spicules. Hollweg, Jackson & Galloway [28] proposed another idea. They studied the dynamical effects of axisymmetric torsional motions propagating in an axisymmetric vertical magnetic flux tube. Their numerical simulations show that magnetohydrodynamic fast shock which is produced in the chromosphere also impel the transition region and underlying chromosphere upward. We considered the situation almost same as Hollweg et al. [28]. However, we imposed random perturbations in the photosphere instead of sinusoidal perturbations assumed by Hollweg et al. [28].

A shape of an open flux tube from the photosphere is assumed to be fixed in a solar atmosphere (Fig.4), although the torsional motion of the tube is allowed (1.5-dimensional approximation) in the cylindrical coordinate. Initially, the atmosphere is stratified in a constant gravity of the solar surface ($g = 2.74 \times 10^4$ cm s^{-2}). The initial transition region is assumed at $\sim$ 2250 km from the photosphere, where the temperature suddenly changes from $\sim$ 5000 K to $\sim 10^6$ K. The strength of the magnetic field is assumed to be $\sim$ 1600 Gauss in the photosphere and $\sim$ 7.8 Gauss in the corona. The specific heat ratio is assumed to be $\gamma = 5/3$. The random perturbation of torque is con-

MHD Shock Tube Values

Variable	Left	FR	IS	CD_l	CD_r	FR	Right
ρ	1.0	0.659	0.823	0.703	0.245	0.116	0.125
		[0.664]	[0.817]	[0.701]	[0.240]	[0.116]	
		(0.676)		(0.697)			
p	1.0	0.434	0.693	0.505	0.505	0.086	0.1
		[0.443]	[0.687]	[0.509]	[0.509]	[0.089]	
		(0.457)		(0.516)			
e	1.0	0.658	0.841	0.718	2.06	0.740	0.8
v_x	0	0.675	0.483	0.601	0.601	-0.280	0
		[0.662]	[0.484]	[0.597]	[0.597]	[-0.255]	
		(0.637)		(0.599)			
v_y	0	-0.252	-1.21	-1.58	-1.58	-0.197	0
		[-0.248]	[-1.16]	[-1.58]	[-1.58]	[-0.179]	
		(-0.233)		(-1.58)			
$B_y/\sqrt{4\pi}$	1.0	0.561	-0.248	-0.536	-0.536	-0.886	-1.0
		[0.567]	[-0.179]	[-0.536]	[-0.536]	[-0.896]	
		(0.585)		(-0.534)			

Table 2: Values in brackets and in parentheses are those given by Stone et al. [25] and by Brio & Wu [19], respectively.

tinually imposed in the photosphere through a calculation. The calculation is performed from t=0 to t=25 minutes. Figure 5 shows the time variation of the density structure along the flux tube. The plots at various time are stacked with time increasing upward in uniform increments of 7.2 second. The transition region is lifted up by nonlinear torsional Alfven waves, and fall down by the gravity. The maximum height is about 5000 km in this case. The upward-moving chromospheric material is observed as spicules.

The advantages of our scheme in this problem are as follows. (1) The CIP method has an advantage of keeping the sharp contact surface. The transition region in the solar atmosphere is the contact surface between the solar corona ($\sim 10^6$ K) and the chromosphere ($\sim 10^4$ K). CIP is useful to distinguish between the solar corona and the chromosphere in the calculations. (2) MOC allows us the stable treatment of discontinuous Alfvén waves. In this problem, the random torque in the photosphere produces discontinuous Alfvén waves. We can detect the energy flux of the Alfvén waves without numerical oscillations.

Our simulation shows the following results. If the root mean square of the random motion is greater than ~ 1 km/s in the photosphere, 1) the transition region is lifted up to more than ~ 5000 km (i.e., the spicule is produced), 2) the energy flux enough for heating the quiet corona ($\sim 3.0 \times 10^5$ erg/s/cm^2) is transported into the corona, and 3) non-thermal broadening of emission lines in the corona is expected to be ~ 20 km/s. The reader is referred to Kudoh & Shibata [29] for more details.

3.2 Simulations of Astrophysical Jets

Astrophysical jets have been observed in young stellar objects (YSOs), active galactic nuclei (AGNs), and some X-ray binaries (XRBs) [30]. Although the acceleration and collimation mechanisms of these jets are still not well understood, these objects are believed to have accretion disks in their central regions. One of the most promising models for jet formation is magnetic acceleration from accretion disks [31, 5, 6] (Fig.6). We here present the results of 1.5D and 2.5D MHD simulations of jet formation by magnetic accretion disks.

3.2.1 1.5D Simulations of Jets

We first show time-dependent 1-dimensional axisymmetric (1.5D) MHD simulations of astrophysical jets

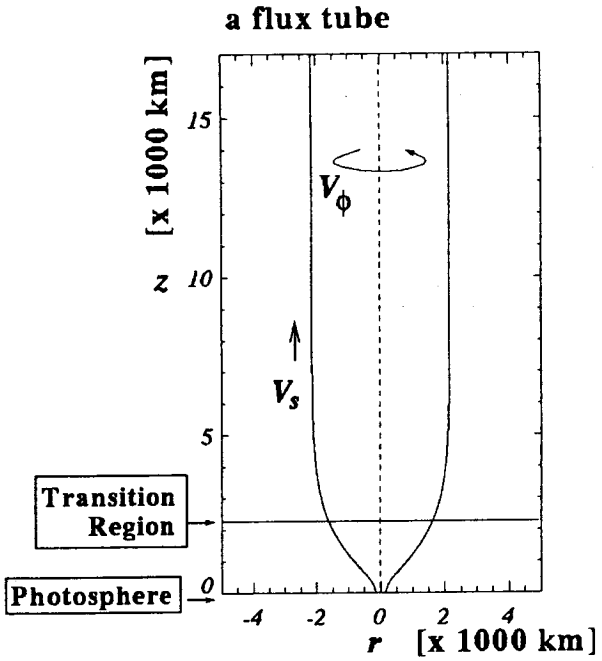

Fig.4: Shape of the flux tube we assumed in the simulations of spicules. The transition region is initially at $z = 2250$ km from the photosphere.

which are magnetically driven from Keplerian disks, assuming a point-mass gravitational potential at the origin.

We study the initial value problem, in which the Keplerian disk threaded by the poloidal magnetic field suddenly begins to rotate and twists the field line, generating "nonsteady jets" by the $J \times B$ force. We have a symmetrical boundary condition at equatorial plane and a free boundary condition at top of the computing region. There are two nondimensional parameters:

$$E_{\rm th} = \frac{V_{s0}^2}{\gamma V_{\rm K0}^2}, \qquad E_{\rm mg} = \frac{V_{\rm A0}^2}{V_{\rm K0}^2}, \qquad (6)$$

where $V_{s0} = (\gamma p_0/\rho_0)^{1/2}$, $V_{\rm A0} = B_0/(4\pi\rho_0)^{1/2}$, $V_{\rm K0} = (GM/r_0)^{1/2}$, p_0 is the initial pressure at the footpoint of the jet, G is the gravitational constant, and M is the mass of a central object. The specific heat ratio is assumed to be $\gamma = 1.2$.

Figure 7a shows the time evolution of the velocity parallel to the poloidal magnetic field v_p. We take the cylindrical coordinate (r, ϕ, z) and it is normalized by r_0 which is the radius of the footpoint of the field line at the equatorial plane. This figure shows that there are two velocity peaks. The leading one is the front of the nonlinear torsional Alfvén wave (*coronal jet*). The

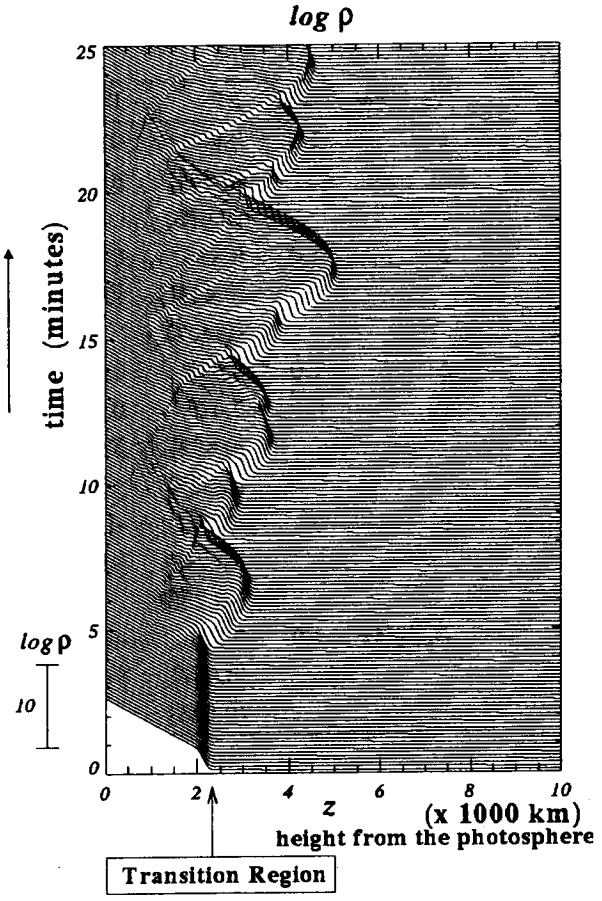

Fig.5: Time variation of density distribution in a spicule. The plots at various time are stacked with time increasing upward in uniform increments of 7.2 second.

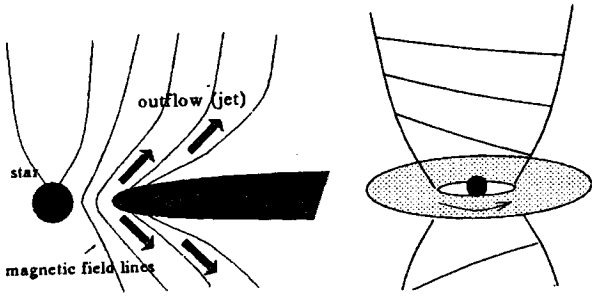

Fig.6: Schematic picture of the magnetically driven jet from an accretion disk. The view of the cross-section on the poloidal plane (left pannel) and the three dimensional view including toroidal component of the magnetic field (right pannel).

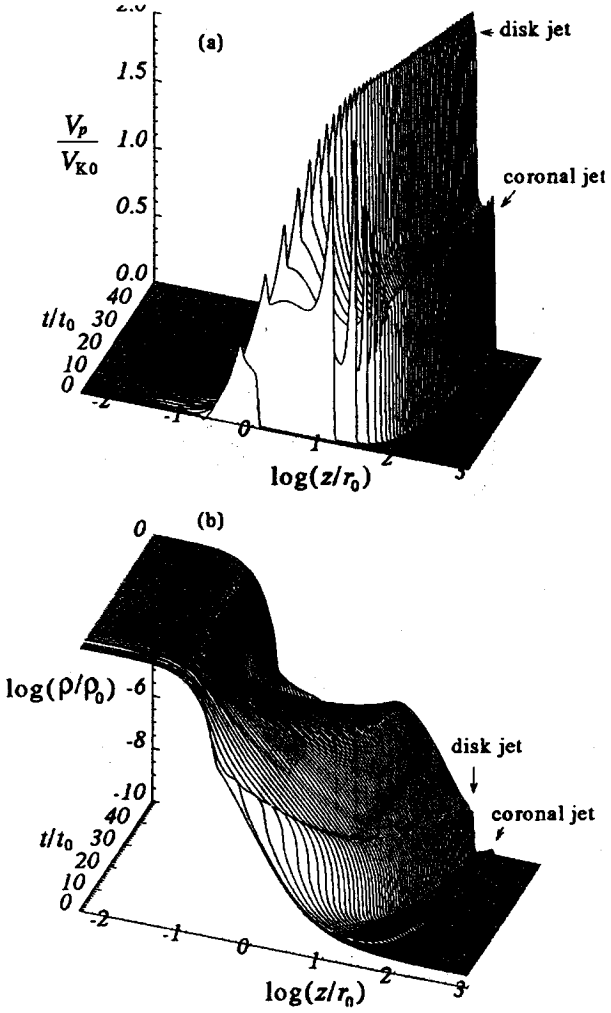

Fig.7: The time variation of (a) the poloidal velocity, and (b) the density of the 1.5D MHD jet from an accretion disk. The velocities are normalized by the Keplerian velocity in the disk. The density is normalized by the initial value at the equatorial plane. The spatial axis z/r_0 is taken as a logarithmic scale. The parameters are $E_{mg} = 1.2 \times 10^{-4}$, and $E_{th} = 6.0 \times 10^{-3}$.

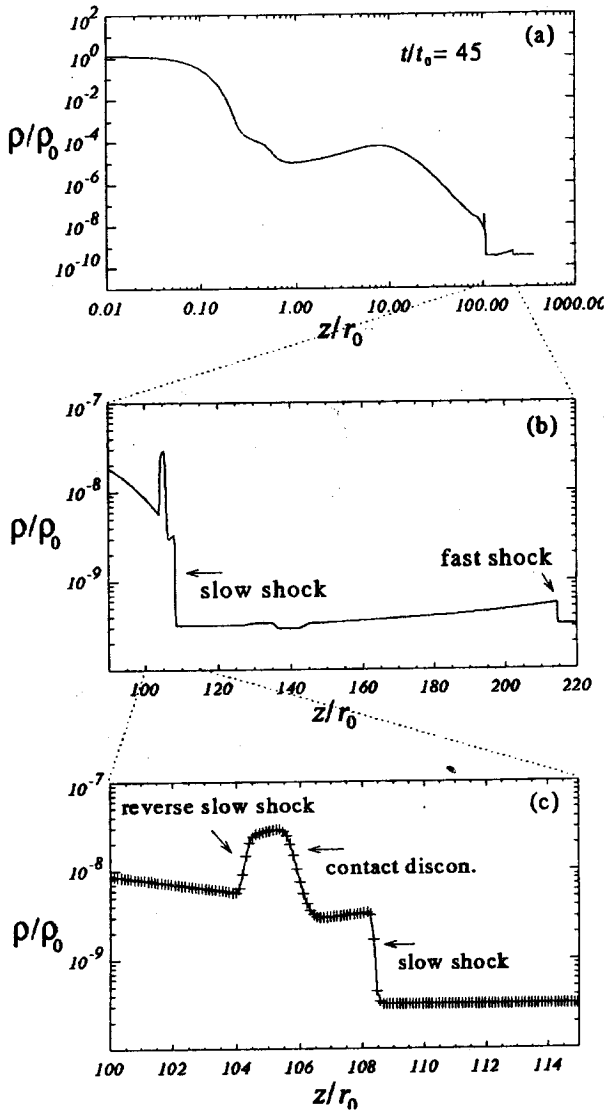

Fig.8: (a) The snapshot ($t/t_0 = 45$) of the density of the 1.5D MHD jet. The parameters are the same as that of Fig.7 (b) The close up view including slow and fast shocks. The spatial axis (z/r_0) is taken as a linear scale. (c)The close up view of the slow shock. We can see the reverse slow shock and the contact discontinuity.

following peak corresponds to the jet which is directly ejected from the disk (*disk jet*). The density evolution (Fig.7b) shows that the mass which is initially in the disk is ejected to the corona, and its front corresponds to the second peak of the velocity. The velocity of the jet is $\sim 2.5V_{K0}$. These two types of jets are the same as those appeared in 2.5-dimensional simulation of Shibata & Uchida [6]. Figure 8 shows the snapshot ($t/t_0 = 45$) of the density distribution along the jet. Figure 8b and 8c are the close up view of Figure 8a. Fast shock, contact discontinuity, slow shock and reverse slow shock are identified.

One of the most important finding in this study

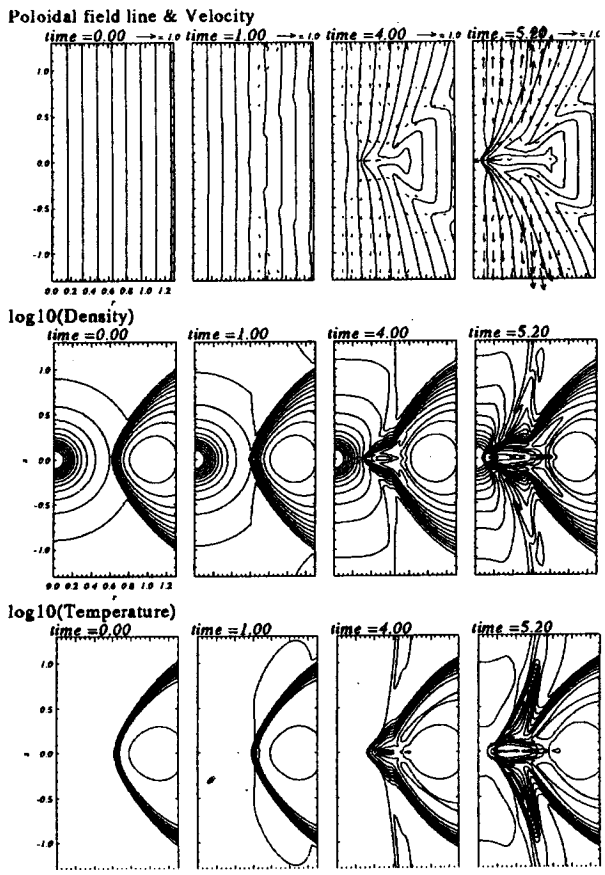

Fig.9: Density, temperature, poloidal magnetic field lines, and poloidal velocity of the 2.5D MHD jet from an accretion disk, calculated with CIP-MOCCT method. Time $t = 2\pi \simeq 6.28$ corresponds to one Keplerian orbit at $(r, z) = (1, 0)$, where length scales are normalized by r_0 where the initial disk density is maximum. Arrows show the poloidal velocity vectors normalized by the Keplerian velocity at $(r, z) = (1, 0)$. The parameters are $E_{\rm mg} \equiv (V_{\rm A0}/V_{\rm K0})^2 = 5.0 \times 10^{-4}$ and $E_{\rm th} \equiv (V_{\rm s0}/V_{\rm K0})^2/\gamma = 0.05$, where $V_{\rm A0}$, $V_{\rm s0}$, and $V_{\rm K0}$ are initial Alfvén velocity, initial sound velocity, and Keplerian velocity at $(r, z) = (1, 0)$, respectively. The grid size is 0.01. The contour step width is 0.25 in logarithmic scale for density, and 0.15 for temperature.

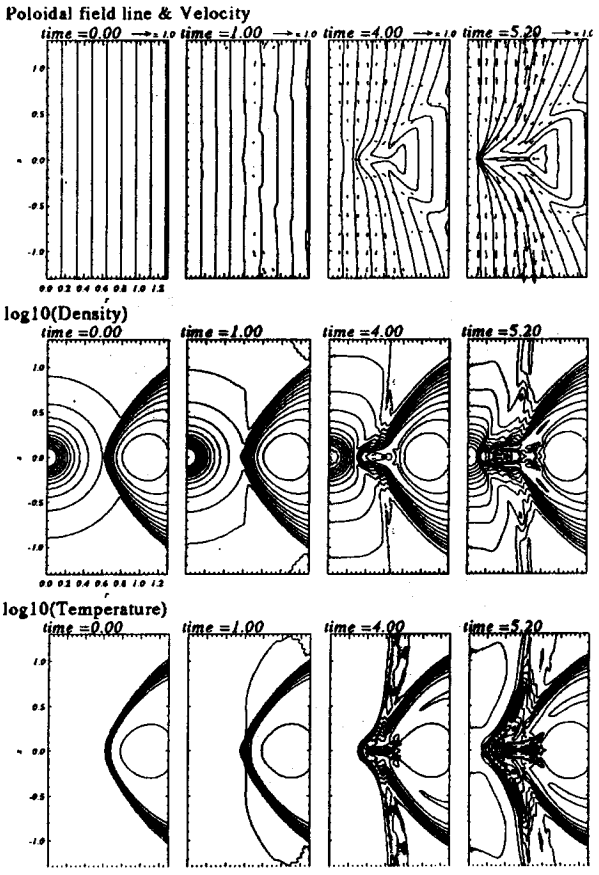

Fig.10: Density, poloidal magnetic field lines, and poloidal velocity, of the 2.5D MHD jet, calculated with modified Lax-Wendroff method. The parameters are the same as those of Fig.9.

is that even when the initial poloidal magnetic field is very weak in the disk (e.g., $E_{\rm mg} \sim 10^{-6}$), a jet with a speed of Keplerian velocity is produced by the effect of magnetic pressure force in the toroidal fields generated from the poloidal fields by the rotation of the disk. The reader is referred to Kudoh & Shibata [32] for more details.

3.2.2 2.5D Simulations of Jets

To investigate the effect of accretion flows in disks, we have performed 2-dimensional axisymmetric (2.5D) MHD simulations of jet formation by magnetic accretion disks in which both ejection and accretion of disk plasma are included self-consistently.

As an initial condition, we assume an equilibrium disk rotating in a central point mass gravitational potential [8]. Exact solutions for these conditions can be obtained under the simplifying assumptions for the distribution of angular momentum and pressure [33]. The mass distribution outside the disk is assumed to be that of uniformly-high temperature corona in hydrostatic equilibrium without rotation. For simplicity, the initial magnetic field is assumed to be uniform and

parallel to the axis of rotation. A mirror symmetrical boundary condition is assumed on the equatorial plane ($z = 0$) and the axis ($r = 0$). The side and top surfaces are free boundaries. In order to avoid a singularity at the origin, the region around $r = z = 0$ is treated by softening the gravitational potential. Two nondimensional parameters ($E_{\rm th}$, $E_{\rm mg}$) are defined as the same manner as those of the 1.5D simulation, except that it is determined at $(r, z) = (1, 0)$. We set $E_{\rm th} = 0.05$ in the simulations. The specific heat ratio is assumed to be $\gamma = 5/3$.

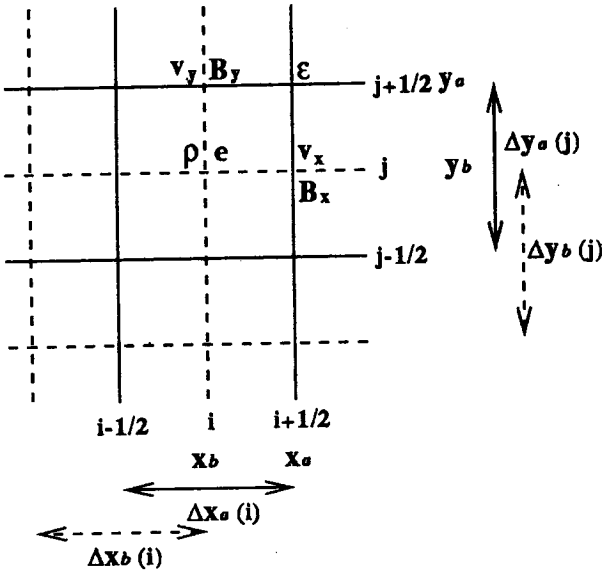

Fig.11: Centering of variables. The density and internal energy density are zone centered, while x- and y- components of velocity and magnetic field are face centered.

Fig.9 shows the time evolution of density, temperature, poloidal magnetic field lines, and poloidal velocity. The initial field strength is $E_{\rm mg} = 5.0 \times 10^{-4}$. Because the magnetic field in the disk is weak, the surface layer of the disk falls faster than the equatorial part [8]. Finally, the material on the disk surface is ejected as a jet by the Lorentz force of the magnetic field.

The result of the numerical simulation shows that the velocity of the jet is of order of the Keplerian velocity of the disk even if the initial magnetic energy is much weaker than the gravitational energy in the disk. This is consistent with the 1.5D simulation shown in the previous section and semi analytical calculation studied by Kudoh & Shibata [34]. The velocities of astrophysical jets in YSOs, AGNs, and XRBs are of order of the escape velocities of the central objects. Our conclusion is that astrophysical jets are ejected from accretion disks which are very close to central stars. The reader is referred to Kudoh, Matsumoto & Shibata [35] for more details.

3.2.3 Comparison with Lax-Wendroff scheme

We compare the results for a magnetically driven jet from an accretion disk using the CIP-MOCCT method and a modified Lax-Wendroff method [36, 37] which was popular among astrophysical MHD simulations. Fig.10 shows the time evolution of density, temperature, poloidal magnetic field lines, and poloidal velocity, which are calculated with the modified Lax-Wendroff scheme. The computational time using the Lax-Wendroff method is about 1.5-2.0 times shorter than that of the CIP-MOCCT method. (When the number of grid points is 345 × 450, the CPU time of CIP-MOCCT method using 1-CPU of VPP300 in National Astronomical Observatory is 10 minutes and 44 seconds with 1000 steps. Both Vectorization and Parallelization are not difficult in our scheme.) Figures 9 and 10 show that (1) the global time evolution with both methods shows good agreement, (2) the contact surface is sharply traced with the CIP-MOCCT method, and (3) numerical oscillations are not prominent when the CIP-MOCCT scheme is used.

In the case of the modified Lax-Wendroff scheme, numerical oscillations appear especially in the jets and in the disk, where the magnetic pressure is larger than the gas pressure (gas pressure/magnetic pressure $< 10^{-2}$). This is caused by the large toroidal component of the magnetic field (B_ϕ) generated by the differential rotation of the disk. Since the equation of total energy is used in the modified Lax-Wendroff scheme, the gas pressure is calculated from the difference between the total energy and the magnetic energy. If the total energy is dominated by the magnetic energy, small numerical oscillations cause the negative pressure which should be eliminated or corrected by some way in order to continue the calculation. In the CIP-MOCCT scheme, we can use the equation of the internal energy instead of the total energy. It avoids this kind of error, and keeps the magnetic energy dominated region without oscillations. In the astrophysical situation, the magnetic pressure often becomes grater than the gas pressure because of the gravitational energy or radiative cooling. Our scheme is suitable for the situation.

On the other hand, the use of the equation of the internal energy does not guarantee the total energy conservation. In the calculations of the CIP-MOCCT scheme, the error of the total energy is about 5%, which is slightly larger than that of the modified Lax-Wendroff scheme (< 3%).

Many results of the CIP-MOCCT scheme show that

the density sometimes becomes very small or negative on the contact surface, in the stagnation region, or in the current sheet. When the density becomes very small, the Alfvén velocity becomes very large and the calculation is stopped by very small time steps. Sometimes, the numerical explosion takes place when the temperature suddenly rises in the grid points where the density becomes very small. Although we have not clarified the reason of this numerical instability, it may be caused by the non-monotonicity of the CIP scheme, the artificial viscosity which is only sensitive to the compression [14], the use of 1D directionally split in MOC method [17], and the mixture of them. We hope that the recent improvements of the schemes [38, 39, 40] may solve this problem.

4 CONCLUSION

We summarize the advantages and the disadvantages of our scheme.

The advantages of our CIP-MOCCT scheme;

- It can trace the contact discontinuity sharply.
- It keeps stable even if the magnetic pressure is much greater than the gas pressure.
- It guarantees $\nabla \cdot \boldsymbol{B} = 0$ within a finite differential form.
- It allows us the stable treatment of the discontinuous Alfvén waves.

The disadvantages of our CIP-MOCCT scheme;

- The total energy conservation is not so good compared with the schemes in which the equations of total energy is used.
- The density sometimes becomes very small or negative on the contact surface, in the stagnation region, or in the current sheet.

Although there are some disadvantages, we conclude that the CIP-MOCCT scheme is practically useful to study astrophysics.

Acknowledgments

The numerical computations were mainly carried out on VPP300/16R and VX/4R at the Astronomical Data Analysis Center of the National Astronomical Observatory, Japan. This work is supported in part by the Grant-in-Aid of the Ministry of Education, Science, Sports and Culture of Japan, 1413 (T.K.) and 07640348 (R.M.).

REFERENCES

[1] K.Shibata, S.Nozawa and R.Matsumoto: Magnetic Reconnection Associated with Emerging Magnetic Flux; Publications of Astronomical Society of Japan, vol.44, pp.265-272, (1992)

[2] T.Yokoyama and K.Shibata: Numerical Simulation of Solar Coronal X-Ray Jets Based on the Magnetic Reconnection Model; Publications of Astronomical Society of Japan, vol.48, p.353-376, (1996)

[3] T.Yokoyama and K.Shibata: Two-dimensional Magnetohydrodynamic Simulation of Chromospheric Evaporation in a Solar Flare Based on a Magnetic Reconnection Model; Astrophysical Journal Letters, vol.494, pp.113-116, (1998)

[4] M.R.Hayashi, K.Shibata and R.Matsumoto: X-Ray Flares and Mass Outflows Driven by Magnetic Interaction between a Protostar and Its Surrounding Disk; Astrophysical Journal Letters, vol.468, p.37-40, (1996)

[5] Y.Uchida and K.Shibata: Magnetodynamical Acceleration of CO and Optical Bipolar Flows from the Region of Star Formation; Publications of Astronomical Society of Japan, vol.37, pp.515-535, (1985)

[6] K.Shibata and Y.Uchida: A Magnetodynamic Mechanism for the Formation of Astrophysical Jets. II - Dynamical Processes in the Accretion of Magnetized Mass in Rotation; Publications of Astronomical Society of Japan, vol.38, pp.631-660, (1986)

[7] S.Hirose, Y.Uchida, K.Shibata and R.Matsumoto: Disk Accretion onto a Magnetized Young Star and Associated Jet Formation; Publications of Astronomical Society of Japan, vol.49, p.193-205, (1997)

[8] R.Matsumoto, Y.Uchida, S.Hirose, K.Shibata, M.R.Hayashi, A.Ferrari, G.Bodo and C.Norman: Radio Jets and the Formation of Active Galaxies. Accretion Avalanches on the Torus by the Effect of a Large-Scale Magnetic Field; Astrophysical Journal, vol.461, pp.115-126, (1996)

[9] S.Tanuma, T.Yokoyama, T.Kudoh, R.Matsumoto, K.Shibata and K.Makishima: Magnetic Reconnection as the Origin of Galactic X-Ray Emission; Publications of Astronomical Society of Japan, vol.51, pp.161-171, (1999)

[10] C.Hirsch: Numerical Computation of Internal and External Flows Wiley-Interscience, Chichester, 1990

[11] D.Ryu, T.W.Jones and A.Frank; Numerical Magnetohydrodynamics in Astrophysics: Algorithm and Tests for Multidimensional Flow; Astrophysical Journal, vol.452, pp.785-796

[12] T.Sano, S.Inutsuka, S.M.Miyama; A Saturation Mechanism of Magnetorotational Instability Due to Ohmic Dissipation; Astrophysical Journal

Letters, vol.506, pp.57-60
[13] N.Fukuda and T.Hanawa: Gravitational and Parametric Instabilities in the Alfvén Wave Traveling Interstellar Medium; Astrophysical Journal, in press, (1999)
[14] T.Yabe and T.Aoki: A Universal Solver for Hyperbolic Equations by Cubic-Polynomial Interpolation I. One-Dimensional Solver; Computer Physics Communications, vol.66, pp.219-232, (1991)
[15] T.Yabe, T.Ishikawa, P.Y.Wang, T.Aoki, Y.Kadota and F.Ikeda: A Universal Solver for Hyperbolic Equations by Cubic-Polynomial Interpolation II. Two- and three-Dimensional Solvers; Computer Physics Communications, vol.66, pp.233-242, (1991)
[16] J.M.Stone and M.L.Norman: ZEUS-2D: A Radiation Magnetohydrodynamics Code for Astrophysical Flows in Two Space Dimensions. II. The Magnetohydrodynamic Algorithms and Tests; Astrophysical Journal Supplement, vol.80, pp.791-818, (1992)
[17] J.Hawley & J.M.Stone: MOCCT: A Numerical Technique for Astrophysical MHD; Computer Physics Communications, vol.89, pp.127-148, (1995)
[18] C.R.Evans and J.F.Hawley: Simulation of Magnetohydrodynamic Flows - A Constrained Transport Method; Astrophysical Journal, vol.332, pp.659-677, (1988)
[19] M.Brio and C.C.Wu: An Upwind Differencing Scheme for the Equations of Ideal Magnetohydrodynamics; Journal of Computational Physics, vol.75, pp.400-422, (1988)
[20] Y.Lin and L.C.Lee: Structure of Reconnection Layers in the Magnetosphere; Space Science Review, vol.65, pp59-179, (1994)
[21] A.A.Barmin, A.G.Kulikovskiy and N.V.Pogorelov: Shock-Capturing Approach and Nonevolutionary Solutions in Magnetohydrodynamics; Journal of Computational Physics, vol.126, pp.77-90, (1996)
[22] A.Zachary and P.Colella: A Higher-Order Godunov Method for the Equations of Ideal Magnetohydrodynamics; Journal of Computational Physics, vol.99, pp.341-347, (1992)
[23] T.Sano: Magnetorotational Instability in Protoplanetary Disks; PhD Thesis, Tokyo University, (1998)
[24] N.Fukuda and T.Hanawa: A Second Order Accurate Numerical Scheme for MHD Equations; in the Proceedings of 'Numerical Astrophysics 1998', in press
[25] J.M.Stone, J.F.Hawley, C.R.Evans, and M.L.Norman: A Test Suite For Magnetohydrodynamical Simulations; Astrophysical Journal, vol.388, pp.415-437, (1992)
[26] J.M.Beckers: Solar Spicules; Annual Review of Astronomy and Astrophysics, vol.10, pp73-100, (1972)
[27] Y.Suematsu, K.Shibata,T.Nishikawa, and R.Kitai: Numerical Hydrodynamics of the Jet Phenomena in the Solar Atmosphere; Solar Physics, vol.75, pp99-118, (1982)
[28] J.V.Hollweg, S.Jackson and D.Galloway: Alfvén Waves in the Solar Atmosphere III. Nonlinear Waves on Open Flux Tubes; Solar Physics, vol.75, pp35-61, (1982)
[29] T.Kudoh and K.Shibata: Alfvén Wave Model of Spicules and Coronal Heating; Astrophysical Journal, vol.514, pp.493-505, (1999)
[30] T.Tajima and K.Shibata: Plasma Astrophysics; Chapter 4.3, pp.353-391, Addison-Wesley, ed. David Pines, (1999)
[31] R.D.Blandford and D.G.Payne: Hydromagnetic Flows from Accretion Discs and the Production of Radio Jets; Monthly Notices of Royal Astronomical Society, vol.199, pp.883-903, (1982)
[32] T.Kudoh and K.Shibata: Magnetically Driven Jets from Accretion Disks. II. Nonsteady Solutions and Comparison with Steady Solutions; Astrophysical Journal, vol.476, pp.612-648, (1997)
[33] M.Abramowicz, M.Jaroszynski and M.Sikora: Relativistic Accreting Disks; Astronomy and Astrophysics, vol.63, pp.221-224, (1978)
[34] T.Kudoh and K.Shibata: Magnetically Driven Jets from Accretion Disks. I. Steady Solutions and Application to Jets/Winds in Young Stellar Objects; Astrophysical Journal, vol.474, pp.362-377, (1997)
[35] T.Kudoh, R.Matsumoto and K.Shibata: Magnetically Driven Jets from Accretion Disks. III. 2.5-dimensional Nonsteady Simulations for Thick Disk Case; Astrophysical Journal, vol.508, pp.186-199, (1998)
[36] E.L.Rubin and S.Z.Burstein: Difference Methods for the Inviscid and Viscous Equations of a Compressible Gas; Journal of Computational Physics, vol.2, pp.178-196, (1967)
[37] T.Yokoyama: Magnetohydrodynamical Simulation of Solar Coronal X-ray Jets Based on Magnetic Reconnection Model; PhD Thesis, The Graduate University for Advanced Studies, (1995)
[38] F.Xiao, T.Yabe, and T.Ito: Constructing Oscillation Preventing Scheme for Advection

Equation by Rational Function; Computer Physics Communications, vol.93, pp.1-12, (1996)
[39] T.Yabe and P.Y.Wang: Unified Numerical Procedure for Compressible and Incompressible Fluid; Journal of the Physical Society of Japan, vol.60, pp.2105-2108, (1991)
[40] D.Clarke: A Consistent Method of Characteristics for Multidimensional Magnetohydrodynamics; Astrophysical Journal, vol.457, pp.291-320, (1996)
[41] B.van Leer: Towards the Ultimate Conservative Difference Scheme.IV. A New Approach to Numerical Convection; Journal of Computational Physics, vol.22, pp.276-299, (1977)
[42] P.Colella and P.R.Woodward: The Piecewise Parabolic Method (PPM) for Gas-Dynamical Simulations; Journal of Computational Physics, vol.54, pp.174-201, (1984)

APPENDIX

We will make a brief introduction of the CIP, CT, and MOC formalism in the Appendix.

4.1 CIP formalism [15]

Consider a 2-dimensional hyperbolic equation,

$$\frac{\partial f}{\partial t} + v_x \frac{\partial f}{\partial x} + v_y \frac{\partial f}{\partial y} = S \tag{7}$$

where f is representative for ρ, v_x, v_y, and e, and S is the the source term, such as pressure gradient, gravity, Lorentz force, and so on.

The spatial derivative of equation (7) gives,

$$\frac{\partial}{\partial t}(\frac{\partial f}{\partial x}) + v_x \frac{\partial}{\partial x}(\frac{\partial f}{\partial x}) + v_y \frac{\partial}{\partial y}(\frac{\partial f}{\partial x}) = \frac{\partial S}{\partial x} - \frac{\partial f}{\partial x}\frac{\partial v_x}{\partial x} - \frac{\partial f}{\partial y}\frac{\partial v_y}{\partial x} \tag{8}$$

$$\frac{\partial}{\partial t}(\frac{\partial f}{\partial y}) + v_x \frac{\partial}{\partial x}(\frac{\partial f}{\partial y}) + v_y \frac{\partial}{\partial y}(\frac{\partial f}{\partial y}) = \frac{\partial S}{\partial y} - \frac{\partial f}{\partial x}\frac{\partial v_x}{\partial y} - \frac{\partial f}{\partial y}\frac{\partial v_y}{\partial y}. \tag{9}$$

These are three equations for three values f, $(\partial f/\partial x)$, and $(\partial f/\partial y)$, and are split into two phases; the non-advection phase (right hand side of the equations) and the advection phase (left hand side of the equations). The CIP scheme is applied to the advection phases of the equations after the non-advection phases are solved with a finite-difference approach.

Non-advection phase

The quantities f, $(\partial f/\partial x)$, and $(\partial f/\partial y)$ are advanced according to

$$f_{ij}^{n+a} = f_{ij}^{n} + S_{ij}\Delta t \tag{10}$$

$$\begin{aligned}(\frac{\partial f}{\partial x})_{i,j}^{n+a} = (\frac{\partial f}{\partial x})_{i,j}^{n} &+ \frac{(f_{i+1,j}^{n+a} - f_{i-1,j}^{n+a} - f_{i+1,j}^{n} + f_{i-1,j}^{n})}{\Delta x_{i+1} + \Delta x_i} \\ &- (\frac{\partial f}{\partial x})_{i,j}^{n} \frac{(v_{x(i+1,j)}^{n} - v_{x(i-1,j)}^{n})\Delta t}{\Delta x_i + \Delta x_{i-1}} \\ &- (\frac{\partial f}{\partial y})_{i,j}^{n} \frac{(v_{y(i+1,j)}^{n} - v_{y(i-1,j)}^{n})\Delta t}{\Delta x_i + \Delta x_{i-1}}\end{aligned} \tag{11}$$

$$\begin{aligned}(\frac{\partial f}{\partial y})_{i,j}^{n+a} = (\frac{\partial f}{\partial y})_{i,j}^{n} &+ \frac{(f_{i,j+1}^{n+a} - f_{i,j-1}^{n+a} - f_{i,j+1}^{n} + f_{i,j-1}^{n})}{\Delta y_{j+1} + \Delta y_j} \\ &- (\frac{\partial f}{\partial x})_{i,j}^{n} \frac{(v_{x(i,j+1)}^{n} - v_{x(i,j-1)}^{n})\Delta t}{\Delta y_j + \Delta y_{j-1}} \\ &- (\frac{\partial f}{\partial y})_{i,j}^{n} \frac{(v_{y(i,j+1)}^{n} - v_{y(i,j-1)}^{n})\Delta t}{\Delta y_j + \Delta y_{j-1}}\end{aligned} \tag{12}$$

where $\Delta x_i = x_{i+1} - x_i$, $\Delta y_j = y_{j+1} - y_j$, $n+a$ on f means the time after one time step in the non-advection phase. In the differential forms of $(\partial S/\partial x)$ and $(\partial S/\partial y)$, S_{ij} is replaced by $(f_{ij}^{n+a} - f_{ij}^{n})/\Delta t$ by using equation (10). We need initial conditions of $(\partial f/\partial x)$ and $(\partial f/\partial y)$ as well as f in the scheme.

For example, the finite differential form of the x-component of the momentum equation (2) in the 2D Cartesian coordinate shown in Figure 11,

$$v_{x(i+1/2,j)}^{n+a} = v_{x(i+1/2,j)}^{n} + S_{i+1/2,j}\Delta t \tag{13}$$

$$\begin{aligned}S_{i+1/2,j} = &-\frac{1}{\rho_{(i+1/2,j)}} \frac{p_{(i+1,j)} - p_{(i,j)}}{\Delta x_{a(i)}} \\ &- \frac{\Psi_{(i+1,j)} - \Psi_{(i,j)}}{\Delta x_{a(i)}} \\ &- \frac{B_{y(i+1/2,j)}}{4\pi\rho_{(i+1/2,j)}} \frac{B_{y(i+1,j)} - B_{y(i,j)}}{\Delta x_{a(i)}} \\ &- \frac{B_{y(i+1/2,j)}}{4\pi\rho_{(i+1/2,j)}} \frac{B^*_{x(i+1/2,j+1/2)} - B^*_{x(i+1/2,j+1/2)}}{\Delta y_{b(j)}},\end{aligned} \tag{14}$$

where $\rho_{(i+1/2,j)} = [\rho_{(i,j)} + \rho_{(i+1,j)}]/2$, $B_{y(i,j)} = [B_{y(i,j+1/2)} + B_{y(i,j-1/2)}]/2$, $B_{y(i+1/2,j)} = [B_{y(i,j+1/2)} + B_{y(i+1,j+1/2)} + B_{y(i,j-1/2)} + B_{y(i+1,j-1/2)}]/4$, and $*$ denotes the value that is calculated with MOC shown later.

Advection phase

In the the advection phase, the advanced quantities f, $(\partial f/\partial x)$, and $(\partial f/\partial y)$ are explicitly written as

$$f^{n+1} = [(A1_{i,j}\xi + A2_{i,j}\eta + A3_{i,j})\xi + A4_{i,j}\eta + (\frac{\partial f}{\partial x})^{n+a}]\xi + [(A5_{i,j}\eta + A6_{i,j}\xi + A7_{i,j})\eta + (\frac{\partial f}{\partial y})^{n+a}]\eta + f_{i,j}^{n+a} \quad (15)$$

$$(\frac{\partial f}{\partial x})^{n+1} = (3A1_{i,j}\xi + 2A2_{i,j}\eta + 2A3_{i,j})\xi + (A4_{i,j} + A6_{i,j}\xi)\xi + (\frac{\partial f}{\partial x})^{n+a} \quad (16)$$

$$(\frac{\partial f}{\partial y})^{n+1} = (3A5_{i,j}\eta + 2A6_{i,j}\xi + 2A7_{i,j})\xi + (A4_{i,j} + A2_{i,j}\xi)\xi + (\frac{\partial f}{\partial y})^{n+a} \quad (17)$$

where $\xi = -v_x^n \Delta t$, $\eta = -v_y^n \Delta t$,

$$A1_{i,j} = [-2d_i + \frac{\partial}{\partial x}(f_{i+1,j}^{n+a} + f_{i,j}^{n+a})\Delta x_i]/(\Delta x_i^3) \quad (18)$$

$$A2_{i,j} = [A8_{i,j} - \frac{\partial d_i}{\partial x}\Delta x_i]/(\Delta x_i^2 \Delta y_j) \quad (19)$$

$$A3_{i,j} = [3d_i - \frac{\partial}{\partial x}(f_{i+1,j}^{n+a} + 2f_{i,j}^{n+a})\Delta x_i]/(\Delta x_i^2) \quad (20)$$

$$A4_{i,j} = [-A8_{i,j} + \frac{\partial d_j}{\partial x}\Delta x_i + \frac{\partial d_i}{\partial y}\Delta y_j]/(\Delta x_i \Delta y_j) \quad (21)$$

$$A5_{i,j} = [-2d_j + \frac{\partial}{\partial y}(f_{i,j+1}^{n+a} + f_{i,j}^{n+a})\Delta y_j]/(\Delta y_j^3) \quad (22)$$

$$A6_{i,j} = [A8_{i,j} - \frac{\partial d_i}{\partial x}\Delta y_j]/(\Delta x_i \Delta y_j^2) \quad (23)$$

$$A7_{i,j} = [3d_j - \frac{\partial}{\partial y}(f_{i,j+1}^{n+a} + 2f_{i,j}^{n+a})\Delta y_j]/\Delta y_j^2 \quad (24)$$

$$A8_{i,j} = f_{i,j}^{n+a} - f_{i+1,j}^{n+a} - f_{i,j+1}^{n+a} + f_{i+1,j+1}^{n+a} \quad (25)$$

$$d_i = f_{i+1,j}^{n+a} - f_{i,j}^{n+a}, \text{ and } d_j = f_{i,j+1}^{n+a} - f_{i,j}^{n+a}. \quad (26)$$

The above equations are derived for $v_x < 0$, $v_y < 0$. We must change: $i+1 \Rightarrow i-1$, and $\Delta x_i \Rightarrow -\Delta x_{i-1}$ for $v_x > 0$, and $j+1 \Rightarrow j-1$, and $\Delta y_j \Rightarrow -\Delta y_{j-1}$ for $v_y < 0$.

4.2 CT formalism [18]

The constrained transport (CT) method maintain $\nabla \cdot \boldsymbol{B} = 0$ constraint. The essential point is the choice of the grid points for magnetic field and electromotive force. For simplicity, we will show the case of 2D Cartesian (x, y) coordinate. In CT formalism, electro-motive force ϵ, which is defined by $\epsilon = -(v_x B_y - v_y B_x)$, is located at the corner of the grid points (Fig.11). From the magnetic induction equation (5), x- and y- components of the equation are

$$\frac{\partial B_x}{\partial t} = -\frac{\partial \epsilon}{\partial y}, \quad \text{and} \quad \frac{\partial B_y}{\partial t} = \frac{\partial \epsilon}{\partial x},$$

respectively. The components of magnetic field are directly advanced by the the finite difference;

$$\frac{1}{\Delta t}[B_{x(i+1/2,j)}^{n+1} - B_{x(i+1/2,j)}^{n}] = -\frac{1}{\Delta y_{a(j)}}[\epsilon_{(i+1/2,j+1/2)} - \epsilon_{(i+1/2,j-1/2)}], \quad (27)$$

$$\frac{1}{\Delta t}[B_{x(i-1/2,j)}^{n+1} - B_{x(i-1/2,j)}^{n}] = -\frac{1}{\Delta y_{a(j)}}[\epsilon_{(i-1/2,j+1/2)} - \epsilon_{(i-1/2,j-1/2)}], \quad (28)$$

$$\frac{1}{\Delta t}[B_{y(i,j+1/2)}^{n+1} - B_{y(i,j+1/2)}^{n}] = \frac{1}{\Delta x_{a(i)}}[\epsilon_{(i+1/2,j+1/2)} - \epsilon_{(i-1/2,j+1/2)}], \quad (29)$$

$$\frac{1}{\Delta t}[B_{y(i,j-1/2)}^{n+1} - B_{y(i,j-1/2)}^{n}] = \frac{1}{\Delta x_{a(i)}}[\epsilon_{(i+1/2,j-1/2)} - \epsilon_{(i-1/2,j-1/2)}]. \quad (30)$$

Equation [(27) $\times \Delta y_{a(j)}$ − (28) $\times \Delta y_{a(j)}$ + (29) $\times \Delta x_{a(i)}$ − (30) $\times \Delta x_{a(i)}$] $\times \Delta t$ shows

$$[B_{x(i+1/2,j)}^{n+1} - B_{x(i+1/2,j)}^{n} - B_{x(i-1/2,j)}^{n+1} + B_{x(i-1/2,j)}^{n}]\Delta y_{a(j)} + [B_{y(i,j+1/2)}^{n+1} - B_{y(i,j+1/2)}^{n} - B_{y(i,j-1/2)}^{n+1} - B_{y(i,j-1/2)}^{n}]\Delta x_{a(i)} = 0. \quad (31)$$

Therefore,

$$\frac{B_{x(i+1/2,j)}^{n+1} - B_{x(i-1/2,j)}^{n+1}}{\Delta x_{a(i)}} + \frac{B_{y(i,j+1/2)}^{n+1} - B_{y(i,j-1/2)}^{n+1}}{\Delta y_{a(i)}} = \frac{B_{x(i+1/2,j)}^{n} - B_{x(i-1/2,j)}^{n}}{\Delta x_{a(i)}} + \frac{B_{y(i,j+1/2)}^{n} - B_{y(i,j-1/2)}^{n}}{\Delta y_{a(j)}}. \quad (32)$$

The equation (32) shows that the finite differential form of $\nabla \cdot \boldsymbol{B} = 0$ is satisfied if it is satisfied in the initial condition. The CT formalism guarantee $\nabla \cdot \boldsymbol{B} = 0$ within finite difference.

4.3 MOC formalism [16]

The MOC allows us the stable treatment of the discontinuous Alfvén waves (see Fig.3).

The Electro Motive Force

The electro motive force in the right hand side of equations (27)-(30) is calculated with MOC;

$$\epsilon = -(v_x^* B_y^* - v_y^* B_x^*) \tag{33}$$

where v_x^*, B_y^*, v_y^*, and B_x^* are calculated from the method of characteristic (MOC) by considering one-dimensional incompressible fluid.

In one-dimensional incompressible fluid in x-direction, the y-component of the momentum equation and the y-component of the induction equation are expressed as

$$\frac{\partial v_y}{\partial t} = \frac{B_y}{4\pi\rho}\frac{\partial B_y}{\partial x} - \frac{\partial}{\partial x}(v_x v_y), \tag{34}$$

$$\frac{\partial B_y}{\partial t} = B_x \frac{\partial v_y}{\partial x} - \frac{\partial}{\partial x}(v_x B_y), \tag{35}$$

respectively. By multiplying equation (35) by $(\sqrt{4\pi\rho})^{-1/2}$ and then adding them,

$$[\frac{\partial}{\partial t} + (v_x + \frac{B_x}{\sqrt{4\pi\rho}})\frac{\partial}{\partial x}](v_y - \frac{B_y}{\sqrt{4\pi\rho}}) = 0, \tag{36}$$

and subtracting them,

$$[\frac{\partial}{\partial t} + (v_x - \frac{B_x}{\sqrt{4\pi\rho}})\frac{\partial}{\partial x}](v_y + \frac{B_y}{\sqrt{4\pi\rho}}) = 0. \tag{37}$$

Equations (36) and (37) are the characteristic equations for Alfvén waves propagating forward and backward, respectively. The finite differential forms of equations of (36) and (37) along the characteristics are

$$(v_y^* - v_y^+) - \frac{1}{\sqrt{4\pi\rho^+}}(B_y^* - B_y^+) = 0, \tag{38}$$

$$(v_y^* - v_y^-) + \frac{1}{\sqrt{4\pi\rho^-}}(B_y^* - B_y^-) = 0, \tag{39}$$

respectively, where $+$ and $-$ denote the value at the footpoints of each characteristic. These two equations for the v_y^* and B_y^* are solved directly, yielding,

$$v_y^* = \frac{v_y^+\sqrt{4\pi\rho^+} + v_y^-\sqrt{4\pi\rho^-} - B_y^+ + B_y^-}{\sqrt{4\pi\rho^+} + \sqrt{4\pi\rho^-}}, \tag{40}$$

$$B_y^* = \frac{-v_y^+ + v_y^- + B_y^+/\sqrt{4\pi\rho^+} + B_y^-/\sqrt{4\pi\rho^-}}{1/\sqrt{4\pi\rho^+} + 1/\sqrt{4\pi\rho^-}}. \tag{41}$$

We set $\rho^+ = \rho_{i-1}^n$ and $\rho^- = \rho_{i+1}^n$ for simplicity. The quantities v_y^+, v_y^-, B_y^+, and B_y^- are calculated as time averaged values obtained by using upwind interpolation at time level n, such as donor cell, van Leer [41] or piecewise parabolic advection [42]. The CIP can be used for this interpolation. We used van Leer interpolation in our code. For example, $v_{y(i+1/2)}^+$ is calculated in the following;

$$v_y^+ = \begin{cases} v_{y(i)}^n + \frac{1}{2}(\Delta x_i - C_{i+1/2}^+\Delta t)\frac{dv_y}{dx}_{(i)} \\ \qquad\qquad \text{if} \quad C_{i+1/2}^+ > 0 \\ v_{y(i+1)}^n - \frac{1}{2}(\Delta x_i + C_{i+1/2}^+\Delta t)\frac{dv_y}{dx}_{(i+1)} \\ \qquad\qquad \text{if} \quad C_{i+1/2}^+ < 0, \end{cases} \tag{42}$$

where $C_{i+1/2}^+ = [v_x - B_x/(\sqrt{4\pi\rho})]_{i+1/2}$ is the characteristic speed of the Alfvén wave propagating forward and,

$$\frac{dv_y}{dx}_{(i)} = \begin{cases} \frac{2\Delta v_{y(i-1/2)}\Delta v_{y(i+1/2)}}{\Delta v_{y(i-1/2)} + \Delta v_{y(i+1/2)}} \\ \qquad \text{if} \quad \Delta v_{y(i-1/2)}\,\Delta v_{y(i+1/2)} > 0 \\ 0 \qquad \text{otherwise}, \end{cases} \tag{43}$$

where $\Delta v_{y(i+1/2)} = (v_{y(i+1)}^n - v_{y(i)}^n)/\Delta x_i$. When we evaluate $C_{i+1/2}^+$, we used velocity which has been advanced in non-advection phase (v_x^{n+a}) in order to get more favorable results in MHD shock tube.

The quantities v_x^* and B_x^* are also calculated in a similar way by solving characteristic equations in a directionally split fashion.

The Stress Term in the Equation of Motion

The MOC method is used to evaluate magnetic field in the stress term of the equation of motion. The finite differential form of the equation (34) in the non-advection phase is

$$\frac{v_{y(i)}^{n+a} - v_{y(i)}^n}{\Delta t} = -\frac{B_x}{4\pi\rho}\frac{B_{y(i+1/2)}^* - B_{y(i-1/2)}^*}{\Delta x}, \tag{44}$$

where v^{n+a} is the updated velocity in the non-advection phase, and B_y^* are the magnetic field that is calculated with MOC. When we calculate B_y^* in the stress term, the characteristic speed in a Lagrangian frame $C^\pm = \mp B_x/\sqrt{4\pi\rho}$ is used instead of $C^\pm = v_x \mp B_x/\sqrt{4\pi\rho}$, because the advection of the equation (34) is calculated with CIP.

In the 2D case, the equation (14) shows that the x-component of the equation of motion has the stress terms in Lorentz force. This is also calculated with MOC. The magnetic pressure terms were calculated with the finite difference of the centered spatial average of magnetic field.